Northumbria Research Link

Carbonaceous Nanomaterial Reinforced Ti-6Al-4V Matrix Composites: Properties, Interfacial Structures and Strengthening Mechanisms

L.L. Dong [a], J.W. Lu [a], Y.Q. Fu [b], W.T. Huo [a], Y. Liu [a], D.D. Li [c], Y.S. Zhang [a, c] *

[a] Advanced Materials Research Central, Northwest Institute for Nonferrous Metal Research, Xi'an 710016, PR China

[b] Faculty of Engineering and Environment, Northumbria University, Newcastle upon Tyne NE1 8ST, UK

[c] Xi'an Rare Metal Materials Institute Co., Ltd, Xi'an, PR China

ABSTRACT:

For conventional titanium matrix composites (TiMCs), there is always a trade-off issue between enhanced strength and ductility of these materials. In this study, we explore a new design methodology by reinforcing titanium alloy matrix with carbonaceous nanomaterials and investigate the mechanisms for achieving a good balance of their strength and ductility. The TiMCs were synthesized through a low-cost powder metallurgy route using pre-mixed Ti-6Al-4V (TC4) powders and various carbon based nanofillers, including graphite powders (GPs), graphene oxide nanosheets (GONs) and graphene nanoplates (GNPs), and were further rolled at a

* Corresponding author: Professor Y.S. Zhang
E-mail: y.sh.zhang@163.com, y.sh.zhang@c-nin.com (Y.S. Zhang)

temperature of 1173 K with a deformation of 66.7%. Among these three types of carbon reinforcing sources, the GNPs are more easily reacted with TC4 matrix and form more contents of TiC phases after sintering owing to their larger amounts of defects than those of the GPs and GONs. TiC products are identified to play a bridging role for not only connecting the TC4 matrix but also forming coherent interfaces with the TC4 matrix, thus facilitating a strong interfacial bonding of the composites. The as-rolled GNPs/TC4 composites exhibit a 0.2% yield strength of 1146.36 MPa (with an elongation of ~8.1%), which is 24.6%, 9.22% and 5.62% higher than those of pure TC4, GPs/TC4 and GONs/TC4 composites. The GNPs/TC4 nanocomposites show a better balance of strength and ductility than those of the other two types of nanocomposites. The synergetic strengthening mechanisms are identified to be Orowan strengthening effect, effective load transfer capability of GNPs, and *in-situ* formation of interfacial TiC structures, which provide optimum interfacial microstructures to achieve good mechanical properties of the TiMCs.

KEYWORDS: Nanocarbon materials, Metal matrix composites, Microstructure, Mechanical properties, Spark plasma sintering

1. INTRODUCTION

Compared to the conventional pure metals (such as Cu, Al, Mg and Ti) and their alloys, metal matrix composites (**MMCs**) have attracted great interest in recent years owing to their excellent physical/mechanical properties (including high strength and

elastic modulus, high hardness, good wear resistance, and good thermal/ electrical properties) [1-10]. For examples, Cu matrix composites are preferred for electrical and tribological applications owing to their good electrical and thermal conductivities [11-13], whereas Al matrix composites are extensively used in aerospace and automotive industries due to their relatively low density and good workability [2, 14-15]. Titanium matrix composites (**TiMCs**) have also found wide-range applications in aerospace, automobile and chemical industries due to their light weight, high specific strength and excellent corrosion resistance [16-18], however, in many applications, their mechanical and physical properties need to be further improved. For this purpose, different 2D or 3D reinforcements such as TiB whiskers, SiC fiber (or particles), TiC, TiN, ZrO_2, Ti_5Si_3, TiB_2 nano/sub-micron particles etc. have been applied as reinforcements [19-26]. For example, Maja et al. [27] reported that the sintered Ti-6Al-4V composites with 4 vol.% TiN showed an indentation hardness value of ~ 7.5 GPa and an elastic modulus of 156 GPa, which are significantly higher than those of Ti-6Al-4V matrix. Huang et al. [28] demonstrated that hot pressing sintered 8.5 vol.% TiB_w/Ti composite with a network microstructure exhibit a large elongation of 11.8% and a strength increment of 74.6%.

Among various reinforcing micro-/nano-materials, carbon nanomaterials are attractive for development of high performance and smart/functional TiMCs for diverse engineering applications, due to their extraordinary mechanical properties (such as high strength and elastic modulus), superior physical properties (e.g., low density, good thermal and electrical properties) and other optical/electrical properties

[29-33] (**see Table 1**). Currently there are a few reports available in literature about the improvement of mechanical properties of pure Ti matrix by introducing graphite powders (**GPs**), graphene nanoplates (**GNPs**) and graphene oxide nanosheets (**GONs**), as listed in **Table S1**. Previously we added 0.3 wt% GONs into pure Ti powders and reported that tensile strength of the sintered TiMC was increased by 9.7%, compared to that of sintered pure Ti matrix [34]. However, none of the reported studies are focused on the reinforcement of Ti alloy matrix using different nanocarbon materials. It is also unclear which carbonaceous nanomaterial could achieve the best strengthening/toughening effects in the Ti alloys matrix, and what the detailed interfacial reactivity/structures between these carbon sources and Ti alloys matrix could be. Understanding these topics will be beneficial for the optimum design and development of new types of titanium matrix composites with a synergistic effect of high strength and good ductility.

Ti-6Al-4V is dominantly used in the aerospace industry because of its excellent mechanical and physical properties [27, 35]. However, compared with other types of high strength titanium alloys (such as Ti-1300 and Ti-1400 [36-37], which are designed and synthesized by Northwest Institute for Nonferrous Metal Research, China), Ti-6Al-4V alloys with their relatively poor strength and ductility often limit their wide-range applications as structural components [38]. In order to solve the above mentioned issues, in this study, we prepare Ti-6Al-4V matrix composites (**TiMCs**) reinforced with three different types of carbon sources i.e. **GPs**, **GONs** and **GNPs**, using low-cost powder metallurgy, effective spark plasma sintering (SPS) and

hot-rolling processes, and then investigate their microstructural characteristics and

mechanical behaviors. This study focuses on an in-depth understanding of interfacial

structures and enhancement mechanisms of these TiMCs, which provide a guidance

for their successful applications into the industry.

Table 1 Various properties of nanocarbon materials. [29-33]

Properties	GPs	GNPs	Carbon Nanofibers
Specific gravity	2.25 g/cm^3	1.8~2.2 g/cm^3	1.8 (AG) ~2.1 (HT) g/cm^3
Resistivity	6000 Ω cm	50 $\mu\Omega$ cm (in-plane)	55(HT)~1000 (AG) $\mu\Omega$ cm
Thermal conductivity	24.0 W m^{-1}K^{-1}	5300 W m^{-1}K^{-1} (in-plane) 6~30 W m^{-1}K^{-1} (c-axis)	20 (AG)~1950 (HT) Wm^{-1}K^{-1}
Transmittance	-	>95% for 2nm thick film >70% for 10nm thick film	-
Elastic modulus	4.8 GPa	0.5~1TPa (in-plane)	0.4 (AG) ~0.6 (HT) TPa
Thermal expansion	0.6~4.3 μm/m-$^{\circ}$C	-1$\times$10^{-6}K^{-1} (in-plane) 29$\times$10^{-6}K^{-1} (c-axis)	-1$\times$10^{-6}K^{-1}(HT; axial)
Specific Surface area	1.0 m^2/g	Typically 100~1000 m^2/g, Up to 2600 m^2/g	10~60 m^2/g
Strength	-	100~400 GPa	2.7 (AG) ~7.0 (HT) GPa
Thickness	-	0.34 nm	-
Thermal stability	< 500 $^{\circ}$C (IA)	450~600 $^{\circ}$C (IA)	450~650 $^{\circ}$C (IA)

*IA=in air, AG=as grown, HT=heat-treated (graphitic)

## 2. EXPERIMANTAL SECTION

2.1 Raw materials

Commercially available Ti-6Al-4V (well-known as **TC4**) powders with an

average size of 75 ~ 150 μm (**Figure 3a**) were purchased from Baoji Haibao Special

Metal Materials Co., Ltd., China. **Table S2** lists the characteristics of TC4 powders

and carbon sources. Their microstructures were characterized using a field emission

scanning electron microscope (**FESEM**, Zeiss GeminiSEM 500) and a

high-resolution transmission electron microscope (**HRTEM**, JEOL JEM-2100Plus)

with selected area electron diffraction (**SAED**). A typical morphology of TC4

spherical powder fabricated using a plasma rotating electrode process is shown in

Figure 3(a).

Graphene nanoplates (**GNPs**) and graphene oxide nanoplates (**GONs**) were

purchased from Nanjing Xian-Feng Nano Materials Technology Co. Ltd., China.

Graphite powders (**GPs**) (＞98% purity, with an average thickness of ~30 nm as

shown in **Figure S1**, and a length/width of ~ 48 μm as shown in **Figures 1(a) ~ 1(c)**)

were supplied from Tianjin Kemiou Chemical Reagent Co., Ltd. China. For

comparisons, **Figures 1(d) to 1(i)** show the morphologies of GONs (with a thickness

of ~10 nm and a length/width ratio of 2~5 μm as shown in **Figure S1**) and GNPs

(with a thickness of ~ 2 nm and a length/width ratio of 1~3 μm as shown in **Figure

S1**). The GPs in **Figure 1(a)** show a rough but thick morphology, nevertheless, the

GONs (**Figure 1d**) and GNPs (**Figure 1g**) show large-scale, thin-layered and

wrinkled structures. Comparing **Figures 1(b~c)** with **Figures 1(d~e)** and **1(h~i)**, we

can see that there are many nanoscale defects existed on the edges of GNPs and

GONs, as marked by arrows in these Figures.
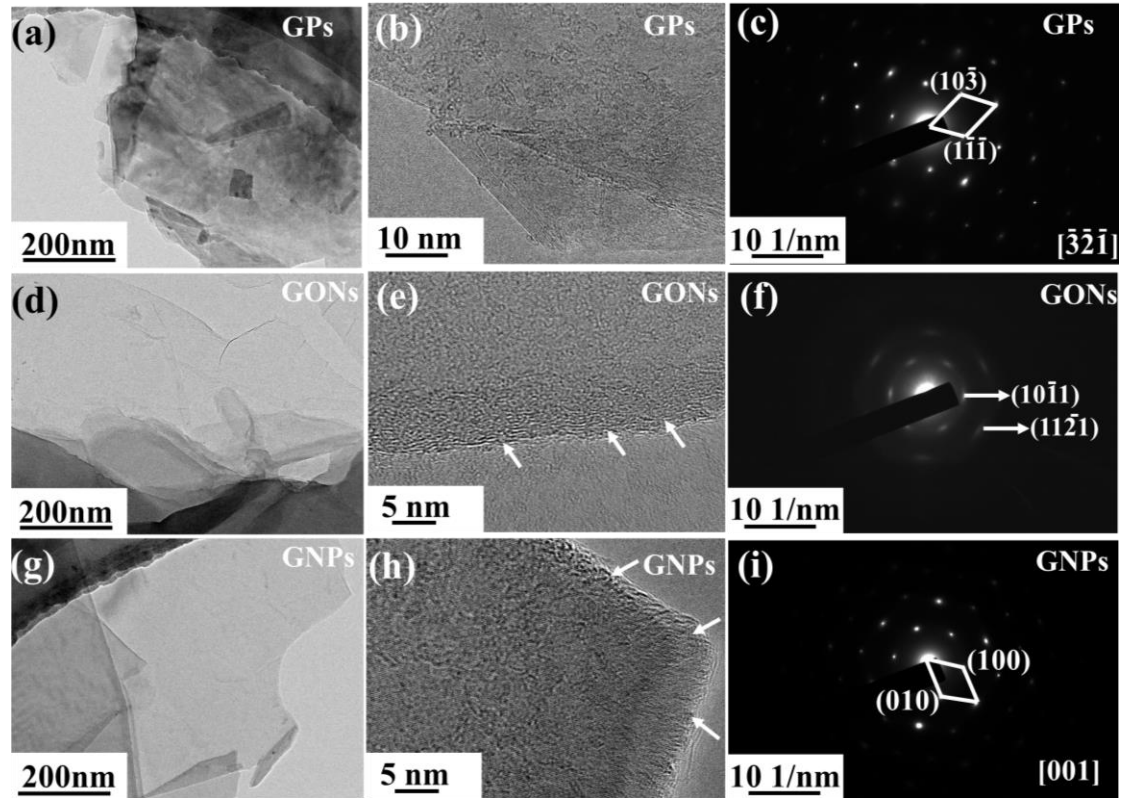
Figure 1. (a) ~ (b) TEM, HRTEM images of GPs and (c) corresponding SAED pattern, (d) ~ (e) TEM, HRTEM images of GONs and (f) corresponding SAED pattern, (g) ~ (h) TEM, HRTEM images of GNPs and (i) corresponding SAED pattern, respectively.

2.2 Fabrication of carbonaceous/TC4 composites

Three different composites, e.g., 0.15 wt% GPs/TC4, 0.15 wt% GONs/TC4 and 0.15 wt% GNPs/TC4 (hereafter, they are named as samples of **GPs/TC4**, **GONs/TC4** and **GNPs/TC4**), were synthesized via a powder metallurgy route as shown in **Figure 2**. The detailed synthesis processes are listed as follows. (1) 0.3 g of carbon sources were added to 300 ml ethanol under an ultrasonic agitation; (2) 200 g of TC4 powders were added into carbon dispersion with the help of ultrasonic and magnetic stirring at

1   a temperature of 323 K; (3) After the above mixed solution was stirred into a semi-dry

2   state, it was then transferred into a stainless steel jar containing stainless steel milling

3   balls with diameters of 2, 5, and 8 mm and a mass ratio of 3: 2: 1. The ball-to-powder

4   weight ratio was 3:1; (4) The jar were agitated using a planetary ball mill at 300 r/min

5   for 5 hours; (5) After mixing, the resulted composite powders was dried at 353 K in a

6   vacuum oven at -0.1 MPa and held for 12 hours.

7

8

9   **Figure 2.** Schematic of preparation of carbonaceous nanomaterials reinforced TC4

10   matrix composites.

11

12   **Figure 3** shows morphologies of the prepared composite powders and the initial

13   TC4 powders. From **Figure 3(a)**, the TC4 powders exhibit spherical shapes with

14   smooth surfaces (**Figure 3a$_1$**). However, the obtained composite powders show much

15   coarser appearance as can be revealed from **Figures 3(b, c, d)**, indicating that the

16   surfaces of TC4 powders are wrapped with GPs (**Figure 3b**), or GONs (**Figure 3c**)

17   and GNPs (**Figure 3d**), respectively. An enlarged view shown in **Figure 3(b$_1$)** reveals

18   that thick flakes of graphite are adhered on the spherical TC4 powders. Whereas

19   **Figures 3(c$_1$) and 3(d$_1$)** show that the GONs and GNPs are not only tightly attached

20   onto the surfaces of TC4 powders, but also quite transparent and crumpled if

21   compared with those shown in **Figure 3(b$_1$)**. This clearly indicates that some of the

22   thin-layered and intact structures of GONs and GNPs are kept after the powder

1 metallurgy processes.

2 Finally, the dried composite powders were loaded into a TZM (with a

3 composition of Mo-0.5%Ti-0.08%Zr-0.0.2%C) die with an internal diameter of 50

4 mm and sintered into the bulk samples in an SPS furnace (**SPS-80T-20**) at 1173 K for

5 5 min of holding time under an axial pressure of 60 MPa. The size of the SPS

6 processed cylinder TiMCs billets was Φ 50 mm$\times$23 mm. Afterwards, a hot rolling

7 process was used to modify and improve morphology and interfacial structures of the

8 composites. Before the hot rolling process, 6 mm thick cylinder samples were

9 obtained via the wire-cutting machine. In this work, hot rolling was performed at 1173

10 K by 66.7% reduction (with four passes) in the thickness direction to obtain fully

11 densified composites with a final thickness of about 2.0 mm.

12

13 **Figure 3.** SEM images of (a) Raw TC4 powders, (b) GPs/TC4 powders, (c)

14 GONs/TC4 powders, (d) GNPs/TC4 powders; (a_1), (b_1), (c_1) and (d_1) are enlarged

15 images of corresponding marked region in Figures 3(a), 3(b), 3(c) and 3(d),

16 respectively.

17

18 **2.3 Characterization**

19 Microstructural characterization of the mixed powders and composites was

20 carried out using an optical microscope (**OM**, Axio Vert A1, ZEISS), an FESEM and

21 a TEM with an energy dispersive spectroscope (**EDS**). SAED and HRTEM were also

22 conducted using the same TEM instrument. The TEM samples of the composites were

prepared by mechanically polishing and ion milling of the sample using a Gatan-691

precision ion polishing system. Prior to performing morphological characterization,

surfaces of the samples were mechanically ground and polished using standard

metallographic procedures. After that, the sample surfaces were etched using the

Kroll's reagent (1 vol.% HF, 3 vol.% HNO_3, and 5 vol.% H_2O [39]) to reveal the

microstructures. The grain sizes of the as-rolled samples were analyzed using the

electron backscatter diffraction (**EBSD**) technique.

Raman spectroscopy was used to investigate structures and defects of carbon

nanomaterials, and this was performed at room temperature using a Laser Raman

Spectrometer (LabRAM HR Evolution) with an excitation wavelength of 532 nm.

X-ray photoelectron spectroscope (**XPS**, Thermo Fisher ESCALAB Xi+) were used to

observe the chemical composition of the carbon source in composites. The size and

morphology of the nanocarbon materials were identified using an atomic force

microscope (**AFM**, Dimension Icon System, Bruker Instruments). Samples for AFM

imaging were prepared by drop-casting the dispersions of carbon nanomaterials onto a

silicon substrate, which was then allowed to dry in air. Electron probe microanalysis

(**EPMA**, JXA-8100, JEOL) were used to investigate the chemical reactions which

have occurred at the interfaces between the nanocarbon sources and TC4 matrix.

Tensile testing specimens were cut along the diameter direction and rolling

direction of the as-sintered/as-rolled samples with a gauge length of 50 mm, a width

of 11 mm and a thickness of 2 mm (**Figure 8b**, inset). The tensile tests were carried

out at room temperature using an MTS810 universal testing machine with a strain rate

of 1 mm/min. At least three measurements were performed in order to acquire an average value. Morphologies and compositions of the fractured surfaces were characterized using the SEM equipped with EDS. In order to study the micro- and nanoscale fracture behavior of the GNPs/TC4 composites, *in-situ* tensile tests were also performed using a miniaturized deformation device within the SEM. The microscale tensile sample was machined from rolled GNPs/TC4 composites into a flat dumbbell shape, which had a gauge length of 6 mm and a cross-section of 2 mm×1 mm. A tiny notch (with a depth of 0.02 mm) was pre-made using wire-electrode cutting on the side of the samples to prepare the fracture position. The prepared microscale sample was further mechanically and electrochemically polished. During the entire tensile tests, the process was paused several times in order to observe the fracture process in real time using the SEM.

3. RESULTS

3.1 Microstructures of carbonaceous materials

Raman spectroscopy is a powerful nondestructive tool to characterize the bonding structures and electronic properties of carbon materials including their disorder and defect structures, defect density and doping levels [40]. The obtained Raman spectra of composite powders and as-sintered samples are shown in **Figure 4**. They all present the characteristic peaks of D band (~1350 cm^{-1}) and G band (~1580 cm^{-1}), which are corresponding to structural defects and degree of graphitization, respectively. Retention of graphene structures in the composites can be confirmed

from the presence and intensity of 2D peak. **Figure S2** shows the fitted Raman peaks

using a Gaussian function, and the obtained results of detailed Raman parameters are

listed in **Table 2**. Raman S_3/2D integral area ratio (i.e. A_{S3}/A_{2D}, which exhibits a

similar tendency with ratio of I_D/I_G) is often used to qualitatively and accurately

evaluate the defect levels of the carbon based materials [41]. Higher value of A_{S3}/A_{2D}

means more defect concentration in the carbon materials, and a lower concentration of

graphene structure is retained if a higher A_{S3}/A_{2D} value is obtained based on the

Raman analysis results. Based on the results shown in **Figure 4** and **Table 2**, the

increased A_{S3}/A_{2D} ratios for the samples of GNPs/TC4 and GPs/TC4 after sintering

can be attributed to the reactions of the GNPs and GPs with TC4 matrix. As listed in

Table 2, the A_{S3}/A_{2D} value of the as-sintered GNPs/TC4 is 0.8746, which is 139.6%

higher than that of the corresponding pre-mixed powders (0.3650). For the as-sintered

GPs/TC4, its A_{S3}/A_{2D} value (0.7847) is 63.6% higher than that of the pre-mixed

GPs/TC4 powders (0.4795). The above results are in a good agreement with their

microstructure characteristics shown in **Figure 1**, where more nanoscale defects

linking with a higher reaction reactivity are found in the GNPs if compared to that of

the GPs. However, for the as-sintered GONs/TC4 sample, a slightly decreased

A_{S3}/A_{2D} value (0.8956) is obtained if compared with that of 0.9584 for the pre-mixed

powders. This is mainly due to the reduction of the GONs into GNPs structure

because of the diminution of oxygen containing functional groups (which has been

verified by the XPS analysis shown in **Figure S3**) during ball milling and sintering

process [42-45]. This can also be confirmed from the weak and broad 2D peaks

(located at ~ 2700 cm^{-1}) of GONs/TC4 sample as shown in **Figures 4(a) and 4(b)**.

Furthermore, by comparing **Figure 4(c)** with **Figures 4(a) and 4(b),** the defect structures of carbon sources in their as-rolled forms were apparently destroyed after rolling, which can be clearly indicated by the increased values of A_D/A_G and A_{S3}/A_{2D} as listed in Table 2 after rolling. It is mainly attributed to the crushed carbon sources under the large rolling forces and formation of TiC after the hot rolling process.

Figure 4. Raman spectra of (a) as-received mixture, (b) SPS and (c) hot rolling processed TiMCs reinforced with three types carbon source, respectively.

Table 2 The detailed Raman spectrum results of samples in this work.

Materials	D band	G band	A_D/A_G	2D band	S3 band	A_{S3}/A_{2D}
GPs/TC4 powders	1354.19	1587.26	0.4563	2713.34	2951.28	0.4795
GONs/TC4 powders	1349.43	1605.75	1.2102	2683.74	2931.74	0.9584
GNPs/TC4 powders	1352.60	1588.81	0.7463	2710.65	2953.39	0.3650
SPSed GPs/TC4	1355.78	1588.81	0.8437	2703.93	2945.05	0.7847
SPSed GONs/TC4	1352.60	1604.21	1.3725	2679.69	2946.08	0.8956
SPSed GNPs/TC4	1352.60	1587.26	0.8933	2721.39	2946.08	0.8746
Rolled GPs/TC4	1350.62	1582.31	1.0923	2694.62	2930.73	0.8350
Rolled GONs/TC4	1350.94	1582.60	1.1156	2693.55	2930.97	0.9267
Rolled GNPs/TC4	1349.35	1587.24	1.2995	2698.94	2932.28	0.9456

EPMA analysis result of the as-sintered composites is shown in **Figure 5**. The analyzed area is ~ 16 μm×12 μm, which contains agglomerated nanocabron materials and *in-situ* formed TiC phases, all embedded inside the TC4 matrix. For the sample of as-sintered TiMCs, a circle of TiC layer was found to form at the interfaces among carbon source and Ti matrix (**Figure 5**). In Figure 5(a), briquets of GPs with a size of

13

1 ~2 μm×4 μm are still remained in the central zone (see carbon mapping in **Figure 5a**)

2 and they have ~ 30% proportion of the marked region in **Figure 5(a)**, comparable to

3 ~33% proportion of the residual GONs of the marked region in **Figure 5(c)**.

4 Furthermore, the EPMA results of GNPs/TC4 shown in **Figure 5(b)** has similar

5 patterns with those of the GPs/TC4 in **Figure 5(a)**, except with some unreacted

6 regions (about 1 μm×1 μm, which is ~ 10% proportion of the marked region in **Figure**

7 **5b**). These results clearly show that the GNPs are much reactive to form TiC with Ti

8 matrix than GONs and GPs at the same process conditions, which are consistent with

9 the Raman spectroscopy results shown in **Figure 4**.

10

11 **Figure 5.** Electron probe microanalysis of TiMCs sintered at 1173 K. (a) GPs/TC4, (b)

12 GNPs/TC4 and (c) GONs/TC4, respectively. For quantitative analysis, the area of

13 remained carbon resources can be estimated from C mappings.

14

15 **3.2 Interfacial structures of TC4-carbonous composites**

16 The interface between the reinforcements and matrix plays a significant role in

17 tailoring the properties of MMCs. **Figure 6** shows the representative three interfacial

18 structures in the GNPs/TC4 composites. There are overlapped and crumpled GNPs

19 phases embedded inside the Ti matrix (**Figure 6a**). Distinct lattice fringes of graphene

20 can be observed from the HRTEM image shown in **Figure 6b**. The lattice parameter

21 was measured to be ~ 0.34 nm, corresponding to the interplanar spacing of graphene

22 (0002) plane. The HRTEM image (**Figure 6i**) of the white square region in Figure 6a

1   shows a distinct GNPs-Ti interface, which confirms the existence of remained GNPs

2   in the matrix. Furthermore, the **SAED** result (**Figure 6b**, inset) reveals that residual

3   GNPs are nearly intact without apparent defects after the sintering, which are similar

4   to those in the previous reports [46-47].

5   **Figure 6(c)** shows that the GNPs structures are completely destroyed in the

6   composite, forming a layer of amorphous carbon film (i.e. destroyed GNPs,

7   confirmed by SAED in **Figure 6f** and EDS of point B) and TiC nanoparticles

8   (denoted by blue arrows and identified by EDS of point C and SAED in **Figure 6e**).

9   EDS results (**Figure 6d**, inset) reveals that the region B contains a high carbon

10   concentration (94.36 at.%, **Table 3**) and extremely low concentration of Ti (4.87 at.%).

11   However, EDS results of region C show that the concentrations of Ti (45.53 at.%) and

12   carbon (53.07 at.%) are nearly equal, suggesting that the nucleation and growth of TiC

13   are preferred to occur with the destructed GNPs. Furthermore, bright-field and

14   dark-field TEM images presented in **Figures 6(c) and 6(d)** demonstrate that the

15   second phase particles are embedded in Ti matrix or at the boundary of the amorphous

16   carbon film. The SAED pattern (**Figure 6e**) obtained from the second phase particles

17   can be indexed as TiC crystals along the [110] direction on the basis of a cubic unit

18   cell.

19   The interfacial structures of amorphous carbon layer and TiC were further

20   studied using HRTEM with one of the obtained images shown in **Figure 6(g)**.

21   Combined with the low magnification TEM image shown in **Figure 6(c)**, it can be

22   concluded that the destroyed GNPs are well bonded with TiC without apparent gaps

and impurities. The noise-filtered IFFT image is shown in **Figure 6(g)** (inset), and the

obtained lattice inter-planar spacing is measured to be ~ 0.26 nm (**Figure 6h**), which

matches the d-spacing of (111) TiC plane. As reported by Chu et al [47], the formed

interfacial carbide nanoparticles can effectively improve the load-bearing ability of

graphene and thus enhance the mechanical properties of the obtained composites.

A transition layer with an average thickness of ~200 nm can be clearly observed

without apparent micro-voids and gaps around the interfaces as shown in **Figure 6(j)**.

Compared with the EDS results listed in **Table 3**, the carbon concentration in this

transition layer is distinctly higher than that in the surrounding matrix. This shows

that the GNPs are mostly reacted with Ti matrix to form TiC, which can be further

confirmed by EDS analysis (e.g., see points of D, E, F in **Figure 6j**). The detailed

interfacial structures between TiC and matrix of GNPs/TC4 were further investigated

using the HRTEM and the results are shown in **Figure 6(k)**. The HRTEM image

reveals that the lattice fringes of TiC (111) intersect with the odd lattice fringes of Ti

(102), having an intersection angle of ~ 77°. The same intersection angle is also

obtained from the Fast Fourier transform (**FFT**) diffraction pattern (**Figure 6k**. inset).

A twin-structure like relationship is observed between Ti (102) and TiC (111) as

shown in the inset of **Figure 6(k)**. This clearly shows that the Ti (102) plane shares its

atomic positions with those of the TiC (111) plane at their interfaces, indicating that

the TiC forms a coherent interface with Ti matrix. It was reported that these coherent

interfaces have lower interface energies if compared with those of incoherent

interfaces [48-49]. Therefore, the formation of these coherent TiC-Ti interfaces should

reduce the interfacial energy and facilitate the generation of strong interfacial bonding

between the TiC particles/layers and Ti matrix.

Figure. 6 TEM and HRTEM images of GNPs/TC4 composites. (a) A bright field

TEM image, white arrows indicate the remained GNPs. (b) HRTEM image and SAED

(inset) of the remained GNPs located near the Ti matrix (region A). (c) A bright field

TEM image showing amorphous carbon (i.e. destroyed GNPs) film and *in-situ* formed

TiC nanoparticles in the GNPs/TC4 composites. Blue arrows show the TiC

nanoparticles. (d) The corresponding dark-field TEM image of the Figure 6(c), inset

showing the EDS result of the TiC (point C) and amorphous carbon (point B). The

SAED of (e) TiC and (f) destroyed GNPs (i.e. amorphous carbon) in Figure 6(c). (g)

HRTEM images of remarked interfacial region in Figure 6(c) and (h) the

corresponding IFFT and lattice spacing measurement recorded at the marked region

of TiC in Figure 6(g), (i) HRTEM image of the interface between TiC and TC4 matrix

(the white square region in Figure 6a), (j) TEM image of the TiC nanolayer in the

composites. (k) HRTEM image of interface and interface relationship between TiC

and Ti matrix, inset showing the IFFT of the interfacial region, respectively.

Table 3 Element compositions and possible phases of the regions marked in Figure 6

(at.%).

Elements	Ti	Al	V	C	Possible phase
A	-	-	-	100	GNPs
B	4.87	0.37	0.40	94.36	Destroyed GNPs
C	45.53	0.75	9.65	53.07	TiC
D	48.39	4.90	3.96	42.75	TiC
E	78.08	12.50	1.23	10.65	Ti
F	77.13	9.43	1.77	11.67	Ti

1

3.3 Mechanical properties and fracture behavior of the composites

Figure 7 shows mechanical properties of the TC4 matrix composites reinforced

with different carbon sources after the SPS (**Figure 7a**) and HR (**Figure 7b**) processes,

and the detailed results are summarized in **Table 4**. Both the 0.2% yield strength

(**0.2% YS**) and ultimate tensile strength (**UTS**) of samples shown in **Figures 7(a)** and

7(b) are increased when different nanocarbon materials are added into the TC4 matrix.

The 0.2% YS of the as-sintered GNPs/TC4 is ~ 980 MPa, which is 27.78% higher

than ~768 MPa of pure TC4 after the SPS process. As a comparison, the as-sintered

composites of GONs/TC4 and GPs/TC4 have 0.2% YS values of ~ 898 MPa and ~

836 MPa, respectively, which are ~ 8.4 and ~ 14.7% lower than that of as sintered

GNPs/TC4.

On the other hand, the elongation of as-sintered TC4 is ~ 15.2% and its fractured

surface shows ductile fracture features with many dimples (**Figure 8a**) and obvious

features of necking (**Figure 8a**, inset). Nevertheless, the elongation values of the

as-sintered TiMCs are all sharply decreased (**Figure 7a and Table 4**). The significant

reduction of elongation values shown in **Figure 7(a)** are attributed to the uncompleted

sintering neck formation. The *in-situ* formed TiC product and the remained

18

nanocarbon materials hinder the rapid diffusion of Ti atoms, thus leading to uncompleted sintering neck formation at the lower temperature. As it is commonly reported [43], formation of these uncompleted sintering necks often results in a low elongation in TiMCs, and relatively poor mechanical properties

These results can also be confirmed by observing the fracture morphologies. **Figures 8(b) to 8(d)** show the original spherical shapes of fractured TC4 and cracks (**as marked in Figure 8b**), also the clusters of nanocarbon materials within the gaps among the TC4 matrices. Results indicate that the main fracture modes of the sintered TiMCs are inter-granular fracture. Furthermore, pulled-out of GNPs can be observed on the fracture surfaces of the as-sintered composites (**Figure 8c$_1$**), suggesting that during the tensile deformation, the load cannot be effectively transferred from the TC4 matrix to the nanocarbons. The appearance of pulled-out of GNPs or GONs also demonstrates interfacial sliding between nanocarbons and TC4 matrix. In addition, clusters of nanocarbon are also observed on the fracture surfaces of the as-sintered composites, which easily lead to crack generation. Both the pulled-out and agglomeration of nanocarbons will severely weaken the strengthening effect.

As shown in **Figure 7 and Table 4**, tensile properties of the as-rolled TiMCs are much better than those of the as-sintered composites. Both the strength and ductility of as-rolled TiMCs shown in **Figure 7(b)** are simultaneously enhanced, which can be attributed to the improvement of bonding between TC4 particles and matrix (**Figures 8f, 8g, and 8h**) and the reinforcements (**Figure S5**) and small sizes of the TC4 matrix (**Figure S6**). For the as-rolled GNPs/TC4 composites shown in **Figure 7(b)**, the

values of 0.2% YS and UTS are increased from ~ 942 MPa and ~ 980 MPa to ~ 1146

MPa and ~ 1269 MPa, which show significant enhancements of 21.7% and 30.5%,

respectively, compared with the as-sintered GNPs/TC4 samples. Meanwhile, the

elongation is also increased up to ~ 350% compared with as-sintered GNPs/TC4

samples. Similar trends can also be observed for the TC4 composites reinforced with

GPs and GONs. The values of 0.2% YS and UTS of GNPs/TC4 composites are

increased up to ~24.6% and ~19% as compared to those of the as-rolled TC4, whereas

those values are 14.1% (17.9%) and 11.0% (12%) for GPs/TC4 (GONs/TC4),

revealing that the GNPs/TC4 composites show a better balance of strength and

ductility than those of the other two nanocomposites, at the similar mass fraction of

carbon nanofillers. The enhanced strengths indicate that GNPs is effective for the

reinforcement in Ti matrix composites.

The fracture surface of the as-rolled GNPs/TC4 shows a typical ductile fracture

mode with a lot of large and deep dimples (**Figure 8g and inset image**), indicating its

good ductility. Instead of being pulled out as shown in those of as-sintered composites,

the nanocarbons in the as-rolled TiMCs can provide a bridging function to connect

TC4 matrix (**Figures 8f$_1$, 8g$_1$ and 8h$_1$**), which improve the load transfer capability of

the composite during deformation.

Figure 7. Engineering stress-strain curves of unreinforced TC4, GPs/TC4,

GONs/TC4 and GNPs/TC4 composites after (a) sintering at 1173 K and (b) HR at

1173 K.

1

Table 4 Tensile properties of as-SPSed and as-Rolled processed TC4 reinforced with

GPs, GONs and GNPs, respectively.

Sample	As-SPSed			As-Rolled		
	0.2% YS (MPa)	UTS (MPa)	Elongation (%)	0.2% YS (MPa)	UTS (MPa)	Elongation (%)
Pure TC4	767.50 ± 12	889.90 ± 8	15.2 ± 0.8	920.03 ± 9	1066.00 ± 13	7.6 ± 1.0
GPs/TC4	835.79 ± 11	963.22 ± 13	3 ± 0.5	1049.56 ± 12	1183.39 ± 10	6.9 ± 1.2
GONs/TC4	897.68 ± 10	951.11 ± 7	5.4 ± 0.6	1085.40 ± 14	1194.06 ± 9	7.0 ± 0.9
GNPs/TC4	941.96 ± 9	979.93 ± 11	1.8 ± 0.3	1146.36 ± 10	1269.66 ± 8	8.1 ± 1.2

4

5

Figure 8. The fracture surface of the TiMCs after (a~d_1) sintering at 1173 K and (e~h_1) HR at 1173 K. (a, e) TC4, (b, b_1, b_2, f, f_1) GPs/TC4, (c, c_1, g, g_1) GNPs/TC4 and (d, d_1, h, h_1) GONs/TC4, respectively. The inset of (b_1), (c_1) and (d_1) shows the EDS mapping of the unreacted nanocarbon materials, and the inset of (f) and (g) exhibits the dimples and tearing ridge, which are the ductile fracture characteristics, the orange inset of (g_1) is the EDS result of in-situ formed TiC, respectively.

To further understand the mechanisms for the improved mechanical properties of the composites, the *in-situ* microscale tensile tests were performed within the SEM in order to observe the real time fracture process of the composites. **Figure 9(a)** shows the photograph of the miniaturized tensile device for the tensile test. A notch was pre-made on the tensile sample to create the stress concentration site (**Figure 9c**), which is helpful for the localized crack initiation during the SEM observation. **Figure**

9(b) presents the load-displacement curve of as-rolled GNPs/TC4 composite with several paused stages of ①~⑥, in each of which the crack propagation was captured using the SEM images, which are shown in **Figures 9(c)~(h)**. It can be seen from **Figure 9(c)** that there is no visible structural change up to the yielding point (stage ①). After yielding, the plastic deformation becomes significant and a crack is initiated from the pre-made notch (stage ②). The crack propagates along a tortuous path (stage ③~⑤) and ultimately leading to the facture of the composite (stage ⑥). The similar crack propagation phenomena have also recently been reported in composites of GNPs/Cu and Ni-CNF/Ti [50-51, 52]. The deflection effect during the crack propagation helps to dissipate more energy and delay the catastrophic crack propagation, thus contributing to the enhanced toughening effect and improved ductility of GNPs/TC4 composites. The *in-situ* microscale tensile test (**Figure S7**) also indicates that the as-rolled GNPs/TC4 composite exhibits a higher strength than that of the as-rolled GPs/TC4 composite, which shows the similar results compared with that from the standard tensile test results shown in **Figure 7**.

To further study failure modes in the as-rolled GNPs/TC4 composites, the magnified SEM images of cracks are also captured during the *in-situ* tensile test. **Figures 9(i)** and **9(j**) reveal that the pulled-out graphene nanoplates are strongly adhered on the fractured matrix, and some deformed TiC particles are also attached to the surface of the matrix. Detailed observation of **Figure 9(j)** shows that that the exposed GNPs are either nearly pulled out from the matrix or display the serrate edges, thus implying the fracture of the GNPs. The pulled-out and fracture phenomena of the

GNPs and deformed TiC particles clearly demonstrate the strong GNPs/TC4 interfacial bonding which can significantly enhance the load transfer capability of GNPs/TC4 composites. Moreover, metal serrations can be observed at the crack tips of the GNPs/TC4 composites (**Figure 9k**), which is a clear evidence of ductile fracture [53]. These metal serrations can effectively restrain the opening of the crack and delay the catastrophic fracture of the composites [54-55], which contribute for the simultaneous enhancement of their strength and ductility.

Figure 9. Fracture behaviors of as-rolled GNPs/TC4 composites based on the *in-situ* microscale tensile test in SEM. (a) Photograph of deformation device installed in the SEM chamber. (b) Load-displacement curve with several paused stages. Inset showing the macrophotograph of the tensile samples before and after in-situ tensile test. (c~h) SEM images of the crack morphology and propagation at the interrupted ①~⑥ stages marked in Figure 9(b). (i) and (j) Magnified image of the fractured surfaces of GNPs/TC4 composites. (k) Presence of metal serrations at the crack tips of the composites, respectively.

4. DISCUSSIONS

4.1 Formation process of interfacial characteristics

Thermodynamic analysis was firstly performed to obtain the Gibbs free energy of carbide formation at the carbonaceous nanomaterials/TC4 matrix interface. For the Ti-C system [56], the possible reactions are:

$$Ti(s) + C(s) = TiC(s) \qquad (1)$$

$$4Ti(s) + 2C(s) = 2Ti_2C(s) \qquad (2)$$
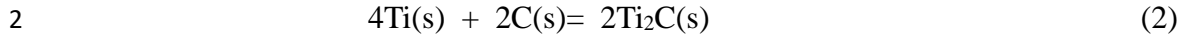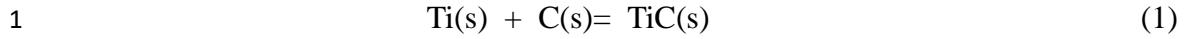
$$\Delta G_1 = -184571.1 + 41.382T + 2.425 \times 10^{-3}T^{-2} - \frac{9.31 \times 10^5}{T} - 5.042T \ln T \ (T < 1939K) \qquad (3)$$

$$\Delta G_2 = -160311.5 - 186.97T - 2.732 \times 10^{-3}T^{-2} - \frac{9.31 \times 10^5}{T} + 24.79T \ln T \ (T > 1939K) \qquad (4)$$

where ΔG (kJ/mol) and T (K) are the Gibbs free energy and the reaction temperature, respectively. Sintering and rolling were all performed at a temperature of 1173 K, and clearly TiC can be easily formed owing to its lower Gibbs free energy (**Figure 10b$_1$**).

Figures 10(a) and **10(b)** schematically show the interface formation mechanisms of the carbonaceous nanomaterial reinforced TC4 matrix composites based on atomic view. Three types carbon sources in this work are used to strengthen the TC4 matrix, but their defects levels and structure integrities of the carbon sources (**Figure 4 and Table 2**) before and after sintering are totally different. Hence, all the carbon sources in the different samples inevitably react with Ti matrix to form TiC phases, where the amount of TiC and reactive level are quite different according to their defects level (confirmed by Raman results in **Figure 4 and Table 2**). For example, the GNPs possess the highest defects level after sintering, therefore, they could easily react with TC4 matrix to form TiC if compared with the other carbon sources. For simplicity, herein we will only focus on the discussions of formation of TiC in the GNPs/TC4 composites.

Previous studies about the Cu matrix composites using reduced oxide graphene (**rGO**) and carbon nanotubues (**CNTs**) as carbon sources have shown that interfacial

24

carbides are preferentially formed at the defective sites of the rGO and CNTs, because of the highly reactive nature of carbon atoms in these defects (pristine and produced) regions, as well as easy formation of carbides [45, 57-59]. Therefore, the defect structures and distribution of carbon sources play critical roles in the nucleation and growth of carbides. As shown in **Figure 1** and **Figure 10(a_1)**, some nanoscale defects are located at edges of the GNPs, which are caused by the oxidation-reduction fabrication process [32]. Furthermore, the defect densities of the GNPs (**Figure S2 and Figure 4**) are slightly increased during the ball milling process owing to the newly generated defects (such as GNPs deformation, fracture, the expansion of the original defect etc.). When the mixed composite powders are rapidly sintered at 1173 K and held for 5 min, some Ti atoms and carbon atoms are inter-diffused, and Ti atoms are quickly diffused to the highly reactive and amorphous carbon defects region, and then react with active carbon atoms of defects region to form TiC particles (**Figure 10b_2**) or TiC layers (**Figure 10b_3**). Meanwhile, some unreacted GNPs are kept and still distributed inside/around the TC4 matrix (**Figure 10b_4**) owing to the short sintering duration. The formed three morphologies at the interfaces in **Figures 10(b_2, b_3 and b_4)** in this work result in a good combination of mechanical performance of the TiMCs reinforced with carbonaceous nanomaterials.

Figure 10. The interface formation mechanism of the TC4 matrix composites reinforced with carbonaceous nanomaterials. (a) The defect of the GNPs' edges based on atomic view, (a_1) TEM and calculated d-spacing of original GNPs, showing the

nanoscale defects, (b) The obtained interfacial structure of the GNPs/TC4 based on atomic view, (b$_1$) comparison of Gibbs free energy of carbides based on HSC chemistry soft 6.0 calculation, (b$_2$) and (b$_3$) the reaction products of Ti and carbon (i.e. GNPs) atoms, and (b$_4$) the remained and distributed GNPs, respectively.

4.2 Strengthening mechanisms

For titanium alloys materials, impurity elements (such as N, O, C) have significant influences on the mechanical properties of the composites, and among them, O and N elements have much higher affinity with Ti matrix than that of C [60]. However, effects of O and N could be neglected in this study. Firstly the low energy milling was employed, and the undamaged spherical shape of the TC4 particles (**Figure 3**) are observed. Secondly the sintering was carried out in a relatively high vacuum atmosphere (10^{-3}~10^{-4}Pa) during the SPS. Texture of the composite would also significantly affect its strength during the rolling. As-rolled TiMCs has normally produced [0001] texture (Figure S6a-d), which is beneficial to the enhancement of their strength [61]. While in this study, the obtained composites exhibit comparable values of Schmid factors with the pure Ti matrix (Figure S6i), indicating that the GNPs and their *in-situ* formed microstructures have insignificant influences on the crystallographic structure of the composites [63]. In fact, the effect of GNPs on the texture could become significant only when their contents are over 0.2 wt.% in the TiMCs [62]. Therefore, we can conclude that texture strengthening induced by carbon sources can be neglected in this study. The similar phenomena has also been reported

26

in other MMCs reinforced with carbonaceous nanomaterials (GNPs, CNTs) in literature [64-65].

Herein, the discussions will be mainly focused on three main strengthening mechanisms of the composites: (1) solution strengthening of carbon atoms; (2) refinement strengthening; and (3) dispersion strengthening and load transfer strengthening of *in-situ* growth of interfacial TiC products and unreacted carbon source.

(1) Strengthening by solution strengthening

Interstitial carbon is an effective strengthening element and carbon atoms are preferably confined to α-phase in an $\alpha+\beta$ titanium alloy. However, further additions of carbon will have minor contribution to the enhancement of strength when the carbon concentrations are above its limit (~ 0.05 wt% for α-Ti at room temperature [66]). As reported in literature, solid solution strengthening (σ_s) by carbon interstitial atoms contributes up to 7 MPa per 0.01 wt% carbon [67]. Based on this, strengthening contribution in 0.2% YS of TiMCs by carbon additions can be calculated as 35 MPa for all TC4 composites containing carbon sources above 0.05wt%. All the results about the strengthening effects in TiMCs have been summarized in **Table 5**.

(2) Strengthening by grain refinement

A reduction of average grain size after sintering improves the strength of metals, which can be described using the Hall-Petch relationship, and the increase of strength ($\Delta\sigma_{GR}$) can be calculated via the following formula [68]:

$$\Delta\sigma_{GR} = K(D_c^{-0.5} - D_m^{-0.5}) \tag{5}$$

27

where K is the Halle-Petch coefficient, and usually shows the average effect of the grain boundaries in the polycrystal, K=0.68 MPa·m$^{1/2}$ [34], D_c and D_m are the average sizes of TiMCs and monolithic TC4 (shown in **Figure S6**), respectively. The calculated $^{\Delta}\sigma_{GR}$ of TiMCs in comparison with that of the pure TC4 alloy are listed in **Table 5**.

(3) Strengthening by TiC and GNPs

As discussed in section 3, there are significant amounts of TiC phases formed during the sintering and rolling process, which consumes the carbon sources in the composite. Therefore, Orowan strengthening and load transfer mechanisms can be used to explain the direct interactions between GNPs or *in-situ* formed TiC particles with the matrix or dislocations in GNPs/TC4 composites (named as σ_{LT-O}), which can be regarded as synthetical contribution from GNPs and TiC. For simplicity, if the tensile strength of TiMCs (σ_c) is regarded as the summation of pure TC4 strength (σ_m), grain refinement (σ_{GR}), solution strengthening (σ_S) and load transfer (σ_{LT-O}), then we can obtain:

$$\sigma_{LT-O} = \sigma_c - \sigma_{GR} - \sigma_m - \sigma_S \tag{6}$$

The obtained strengthening contribution of the σ_m, σ_{GR}, σ_S and σ_{LT-O} are summarized in **Figure 11**. It can be seen that the grain refinement is contributed to a small portion (2.3 ~ 6.7 MPa) to the composites, and the Orowan strengthening and load transfer of TiC and carbon sources are dominant for the enhanced strength. When the GNPs are introduced in TC4 matrix, the enhanced strength by the Orowan strengthening and load transfer strengthening is 184.6 MPa (obtained using Eq. 6),

substantially higher than that of GONs/TC4 (128.06 MPa) and GPs/TC4 (92.19 MPa).

Therefore, it can be concluded that the GNPs show the maximum strengthening effect in TiMCs. The defects of GNPs edges (**Figure 1 and Figure 4**) can provide the most active sites for the formation of TiC particles/layers, thus resulting in coherent interfaces and good interfacial bonding as well as high strength of GNPs. GONs also shows the similar nanoscale defects sites, however their defect levels are decreased during the sintering process [43] (shown in **Figure 4 and Table 2**). As for GPs/TC4 composites, the GPs have a layered structure with multiple graphene sheets bonded by a weak Wan der Waals force. Moreover, their mechanical and physical properties across the basal plane (i.e., through thickness direction) are inferior to those obtained along the basal plane [69], leading to weaker bonding compared with TiMCs reinforced using GNPs as carbon sources. Therefore, the GPs/TC4 composites possess the lowest strength among three TiMCs.

Figure 11. Comparisons of strengthening factors TiMCs in composites.

Table 5 Mechanical strengthening mechanism of as-rolled TiMCs.

Materials	Grain size (μm)	Grain refinement (MPa)	Orowan strengthening and load transfer by TiC and residual carbon sources (MPa)	Strengthening by carbon solution strengthening (MPa)	0.2% YS (MPa)	Increased 0.2% YS (MPa)
TC4	3.009	0	0	0	920.03	0
0.15GPs/TC4	2.516	2.34	92.19	35	1049.56	129.53
0.15GNPs/TC4	2.434	6.73	184.60	35	1146.36	226.33
0.15GONs/TC4	2.538	2.31	128.06	35	1085.40	165.37

5. CONCLUSIONS

In summary, graphite powders, graphene oxides and graphene nanoplates were employed as reinforcements to fabricate the TiMCs using powder metallurgy and hot rolling processes. The residual carbon sources, TiC nanoparticles/layer are simultaneously found in the composites, while their proportions depend on internal defects and reaction activity with TC4 matrix. All the three types carbonaceous nanofillers significantly improve the mechanical properties of the TiMCs. Especially, GNPs/TC4 composites show a better balance of strength and ductility than the other two composites, at the similar mass fraction of carbon nanofillers. The as-rolled GNPs/TC4 composites exhibits a 0.2% YS and UTS of ~1146 MPa and 1269 MPa, which have been increased by ~ 24.6% and ~ 19% as compared to those of the as-rolled TC4, as well as a good elongation of 8.1%. The enhanced strength is linked closely with the defect density and the formation of coherent TiC-Ti interfaces. The synergetic strengthening effect due to the Orowan strengthening and load transfer of GNPs and *in-situ* formation of interfacial TiC phases have significantly contributed to the enhanced strength of the TiMCs.

ASSOCIATED CONTENT

Supporting Information

Supporting Information is available from the Elsevier Publications or from the author.

AUTHOR INFORMATION

Corresponding Author: Y.S. Zhang

Notes

The authors declare no competing financial interest.

REFERENCES

[1] L.L. Dong, M. Ahangarkani, W.G. Chen, Y.S. Zhang, Recent progress in development of tungsten-copper composites: fabrication, modification and applications, Int. J. Refract. Metal. H. Mat. 75 (2018) 30–42.

[2] G.H. Wu, Z.H. Yu, L.T. Jiang, C. Zhou, G. Deng, X.B. Deng, Y.Z. Xiao, A novel method for preparing graphene nanosheets/Al composites by accumulative extrusion-bonding process, Carbon 152 (2019) 932-945.

[3] H.G. Prashantha Kumar, M. Anthony Xavior, Effect of graphene addition on flexural

properties of al 6061 nanocomposites, Materials today Proc. 4(8) (2017) 8217-8133.

[4] A. Ekramia, F. Shahrib, A. Miraka, Effect of rare-earth elements and quenching wheel speed on the structure, mechanical and thermal properties of rapidly solidified AZ91 Mg melt-spun ribbons, Mat. Sci. Eng. A 684(2017) 586-591.

[5] G.Q. Han, J.H. Shen, X.X. Ye, B. Chen, H. Imai, K. Kondoh, W.B. Du, The influence of CNTs on the microstructure and ductility of CNT/Mg composites, Mater. Lett. 181 (2016) 300-304.

[6] L. Bolzoni, F. Yang, Development of Cu-bearing powder metallurgy Ti alloys for biomedical Applications, J. Mech. Behav. Biomed. 97 (2019) 41–48.

[7] L. Bolzoni, E. Herraiz, E.M. Ruiz-Navas, E. Gordo, Study of the properties of low-cost powder metallurgy titanium alloys by 430 stainless steel addition, Mat. Des. 60 (2014) 628–636.

[8] M. Bastwros, G.Y. Kim, C. Zhu, K. Zhang, S.R. Wang, X.D. Tang, X.W. Wang, Effect of ball milling on graphene reinforced Al6061 composite fabricated by semi-solid sintering, Compos. Part B 60 (2014) 111–118.

[9] P. DevSrivyas, M.S.Charoo, Role of fabrication route on the mechanical and tribological behavior of aluminum metal matrix composites – A Review, Materials today: Proc. 5(2018) 20054-20069.

[10] Y.J. Liu, Y.S. Zhang, L.C. Zhang, Transformation-induced plasticity and high strength in beta titanium alloy manufactured by selective laser melting, Materialia 6 (2019) 100299.

[11] A. Karthikeyan, S. Coulombe, A.M Kietzig, Robin S. Stein, Theo van de Ven, Interaction of oxygen functionalized multi-walled carbon nanotube nanofluids with copper, Carbon 140 (2018) 201-209.

[12] K. Chu, X.H. Wang, Y.B. Li, D.J. Huang, Z.R. Geng, X.L. Zhao, H. Liu, H. Zhang, Thermal properties of graphene/metal composites with aligned graphene, Mat. Des. 140 (2018) 85–94.

[13] K. Chu, X.H. Wang, F. Wang, Y.B. Li, D.J. Huang, H. Liu, W.L. Ma, F.X. Liu, H. Zhang, Largely enhanced thermal conductivity of graphene/copper composites with highly aligned graphene network, Carbon 127 (2018) 102-112.

[14] A. Canakci, T. Varol, Microstructure and properties of AA7075/Al–SiC composites fabricated using powder metallurgy and hot pressing. Powder Technol. 268 (2014) 72-79.

[15] A. Azarniya, H.R.M. Hosseini, M. Jafari, N. Bagheri, Thermal decomposition of nanostructured Aluminum Titanate in an active Al matrix: a novel approach to fabrication of in situ Al/Al_2O_3–Al_3Ti composites, Mat. Des. 88 (2015) 932–941.

[16] J.W. Lu, Y.Q. Zhao, H.Z. Niu, Y.S. Zhang, Y.Z. Du, W. Zhang, W.T. Huo, Electrochemical corrosion behavior and elasticity properties of Ti–6Al–xFe alloys for biomedical applications, Mat. Sci. Eng. C 62 (2016) 36-44.

[17] J.C. Williams, E.A. Starke, Progress in structural materials for aerospace systems, Acta Mater. 51 (2003) 5775–5779.

[18] Y. Jiao, L.J. Huang, L. Geng, Progress on discontinuously reinforced titanium matrix composites, J. Alloy. Compd. 767 (2018) 1196-1215.

[19] K. Geng, W.J. Lu, D. Zhang, T. Sakata, H. Mori, Tensile properties of in situ synthesized titanium matrix composites reinforced by TiB and Nd_2O_3 at elevated temperature, Mat. Des. 24 (2003) 409–414.

[20] Y. Yu, W.C. Zhang, W.Q. Dong, X.Z. Han, C.L. Pei, X.Y. Jiao, Y.J. Feng, Research on heat treatment of TiB_w/Ti6Al4V composites tubes, Mat. Des. 73 (2015) 1–9.

[21] E. Ghasali, M.S. Asl, Microstructural development during spark plasma sintering of ZrB$_2$–SiC–Ti composite, Ceram. Int. 44(2018) 18078-18083.

[22] J.W. Lu, Y.Q. Zhao, Y, Du, W. Zhang, Y.S. Zhang, Microstructure and mechanical properties of a novel titanium alloy with homogeneous (TiHf)$_5$Si$_3$ particle-reinforcements, J. Alloy. Compd. 778 (2019) 115-123.

[23] A.S. Patil, V.D. Hiwarkar, P.K. Verma, R.K. Khatirkar, Effect of TiB$_2$ addition on the microstructure and wear resistance of Ti-6Al-4V alloy fabricated through direct metal laser sintering (DMLS), J. Alloy. Compd. 777 (2019) 165-173.

[24] A.P.I. Popoola, L. Phume, S. Pityana, V.S. Aigbodion, In-situ formation of laser Ti6Al4V-TiB composite coatings on Ti6Al4V alloy for biomedical application, Surf. Coat. Technol. 285 (2016) 161-170.

[25] L. Huang, L. Wang, M. Qian, J. Zou, High tensile-strength and ductile titanium matrix composites strengthened by TiB nanowires, Scr. Mater. 141 (2017) 133-137.

[26] Y. Jiao, L.J. Huang, L. Geng, X.T. Li, Y.N. Gao, M.F. Qian, R. Zhang, Nano-scaled Ti$_5$Si$_3$ evolution and Strength Enhancement of titanium matrix composites with two-scale architecture via heat treatment, Mat. Sci. Eng. A 701 (2017) 359–369.

[27] M.E. Maja, O.E. Falodun, B.A. Obadele, S.R. Oke, P.A. Olubambi, Nanoindentation studies on TiN nanoceramic reinforced Ti–6Al–4V matrix composite, Ceram. Int. 44 (2018) 4419–4425.

[28] L.J. Huang, S. Wang, Y.S. Dong, Y.Z. Zhang, F. Pan, L. Geng, H.X. Peng, Tailoring a novel network reinforcement architecture exploiting superior tensile properties of in situ TiB$_w$/Ti composites, Mat. Sci. Eng. A 545 (2012) 187– 193.

[29] B. Z. Jang, A. Zham, Processing of nanographene platelets (NGPs) and NGP nanocomposites:

a review, J. Mater. Sci. 43 (2008) 5092–5101.

[30] X.M. Anthony, H.G. Prashantha Kumar, Processing and characterization techniques of graphene reinforced metal matrix composites (GRMMC); A Review, Materials Today: Proc. 4 (2017) 3334–3341.

[31] H.C. Lee, W.W. Liu, S.P. Chai, A.R. Mohamed, C.W. Lai, C.S. Khe, C.H. Voon, U. Hashim, N.M.S. Hidayah, Synthesis of single-layer graphene: A review of recent development, Proc. Chem. 19 (2016) 916 – 921.

[32] L.L. Dong, W.G. Chen, N. Deng, C.H. Zheng, A novel fabrication of graphene by chemical reaction with a green reductant, Chem. Eng. J. 306 (2016) 754–762.

[33] L.L. Dong, Y.C. Ding, W.T. Huo, W. Zhang, J.W. Lu, L.H. Jin, Y.Q. Zhao, G.H. Wu, Y.S. Zhang, A green and facile synthesis for rGO/Ag nanocomposites using one-step chemical co-reduction route at ambient temperature and combined first principles theoretical analyze, Ultrason. Sonochem. 53 (2019) 152–163.

[34] L.L. Dong, B. Xiao, L.H. Jin, J.W. Lu, Y. Liu, Y.Q. Fu, Y.Q. Zhao, G.H. Wu, Y.S. Zhang, Mechanisms of simultaneously enhanced strength and ductility of titanium matrix composites reinforced with nanosheets of graphene oxides, Ceram. Int. 4(2019) 19370-19379.

[35] G. Lutjering, J.C. Williams, Titanium, Second edition, springer, 2003, 383-413.

[36] J.W. Lu, Y.Q. Zhao, P. Ge, H.Z. Niu, Y.S. Zhang, W. Zhang, P.X. Zhang, Microstructure and mechanical properties of new high strength beta-titanium alloy Ti-1300, Mat. Sci. Eng. A 621 (2015) 182-189.

[37] J.W. Lu, P. Ge, Q. Li, W. Zhang, W.T. Huo, J.J. Hu, Y.S. Zhang, Y.Q. Zhao, Effect of microstructure characteristic on mechanical properties and corrosion behavior of new high

strength Ti-1300 beta titanium alloy, J. Alloy. Compd. 727(2017) 1126-1135.

[38] V.A.R. Henriques, P.P.D. Campos, C.A.A. Cairo, and J.C. Bressiani, Production of Titanium

alloys for advanced aerospace systems by powder metallurgy, Mat. Res. 8(2005) 443–446.

[39] J.W. Lu, X.R. Yang, Y.Q. Zhao, L.L. Dong, Y.Q. Fu, Y. Du, W. Zhang, Y.S. Zhang, Influence

of as precipitates on electrochemical performance and mechanical degradation of Ti-1300 alloy, J.

Alloy. Compd. 803(2019) 88-101.

[40] J. Ribeiro-Soares, M.E. Oliveros, C. Garin, M.V. David, L.G.P. Martins, C.A. Almeida, E.H.

Martins-Ferreira, K. Takai, T. Enoki, R. Magalh~aes-Paniago, A. Malachias, A. Jorio, B.S.

Archanjo, C.A. Achete, L.G. Cançado, Structural analysis of polycrystalline graphene systems by

Raman spectroscopy, Carbon 95 (2015) 646-652.

[41] A.C. Ferrari, D. M. Basko, Raman spectroscopy as a versatile tool for studying the properties

of graphene, Nat. Nanotechnol. 8 (2013) 235-246.

[42] I.Y. Jeon, H.J. Noh, J.B. Baek, Direct and efficient conversion from low-quality graphite to

high-quality graphene nanoplatelets, FlatChem, 12 (2018) 10-16.

[43] L.L. Dong, B. Xiao, Y. Liu, Y.L. Li, Y.Q. Fu, Y.Q. Zhao, Y.S. Zhang, Sintering effect on

microstructural evolution and mechanical properties of spark plasma sintered Ti matrix

composites reinforced by reduced graphene oxides, Ceram. Int. 44 (2018) 17835–17844.

[44] L.L. Dong, W.G. Chen, C.H. Zheng, N. Deng, Microstructure and properties characterization

of tungsten-copper composite materials doped with graphene, J. Alloy. Compd. 695 (2017)

1637-1646.

[45] L.L. Dong, W.T. Huo, M. Ahangarkani, B. Zhang, Y.Q. Zhao, Y.S. Zhang, Microstructural

evaluation and mechanical properties of in-situ WC/W-Cu composites fabricated by rGO/W-Cu

spark plasma sintering reaction, Mat. Des.160 (2018) 1196–1207.

[46] X.N. Mu, H.N. Cai, H.M. Zhang, Q.B. Fan, Z.H. Zhang, Y. Wu, Y.X. Ge, D.D. Wang, Interface evolution and superior tensile properties of multi-layer graphene reinforced pure Ti matrix composite, Mat. Des. 140 (2018) 431–441.

[47] K. Chu, J. Wang, Y.P. Liu, Z.R. Geng, Graphene defect engineering for optimizing the interface and mechanical properties of graphene/copper composites, Carbon 140 (2018) 112-123.

[48] K. Chu, F. Wang, Y.B. Li, X.H. Wang, D.J. Huang, Z.R. Geng, Interface and mechanical/thermal properties of graphene/copper composite with Mo_2C nanoparticles grown on graphene, Compos. Part A 109 (2018) 267–279.

[49] X. Mao, K.H. Oh, J. Jang, Evolution of ultrafine grained microstructure and nano-sized semi-coherent oxide particles in austenitic oxide dispersion strengthened steel, Mater. Charact. 117 (2016) 91–98.

[50] D.B. Xiong, M. Cao, Q. Guo, Z.Q. Tan, G.L. Fan, Z.Q. Li, D. Zhang, Graphene-and-copper artificial nacre fabricated by a preform impregnation process: bioinspired strategy for strengthening-toughening of metal matrix composite, ACS Nano 9 (2015) 6934-6943.

[51] K. Chu, J. Wang, Y.P. Liu, Y.B. Li, C.C. Jia, H. Zhang, Creating defects on graphene basal-plane toward interface optimization of graphene/CuCr composites, Carbon 143 (2019) 85-96.

[52] X.N. Mu, H.N. Cai, H.M. Zhang, Q.B. Fan, F.C. Wang, Z.H. Zhang, Y.X. Ge, R. Shi, Y. Wu, Z. Wang, D.D. Wang, S. Chang, Uniform dispersion and interface analysis of nickel coated graphene nanoflakes/ pure titanium matrix composites, Carbon 137 (2018) 146-155.

[53] S. Cheng, E. Ma, Y.M. Wang, L.J. Kecskes, K.M. Youssef, C.C. Koch, U.P. Trociewitz, K.

Han, Tensile properties of in situ consolidated nanocrystalline Cu, Acta Mater. 53 (2005) 1521-1533.

[54] Y. Zhang, X.C. Li, Bio-inspired, graphene/Al_2O_3 doubly reinforced aluminum composites with high strength and toughness, Nano Lett. 17 (2017) 6907-6915.

[55] L. Meng, X. Wang, J. Ning, X. Hu, G. Fan, K. Wu, Beyond the dimensional limitation in bio-inspired composite: insertion of carbon nanotubes induced laminated Cu composite and the simultaneously enhanced strength and toughness, Carbon 130 (2018) 222-232.

[56] H.M. Ding, W.W. Chu, Q. Liu, H.Q. Wang, C. Hao, H.R. Jia, J.F. Wang, T.J. Ci, Microstructure evolution of Cu-TiC composites with the change of Ti/C ratio, Results Phys. 14 (2019) 102369-102377.

[57] N. Xiong, R. Bao, J.H. Yi, J.M. Tao, Y.C. Liu, D. Fang, Interface evolution and its influence on mechanical properties of CNTs/CuTi composite, Mat. Sci. Eng. A 755 (2019) 75–84.

[58] K. Chu, F. Wang, X.H. Wang, Y.B. Li, Z.R. Geng, D.J. Huang, H. Zhang, Interface design of graphene/copper composites by matrix alloying with titanium, Mat. Des. 144 (2018) 290–303

[59] A.M.K. Esawi, K. Morsi, A. Sayed, M. Taher, S. Lanka, Effect of carbon nanotube (CNT) content on the mechanical properties of CNT-reinforced aluminium composites, Compos. Sci. Technol. 70 (2010) 2237–2241.

[60] J.C. Williams, A.F. Belov, eds.: Titanium and Titanium Alloys, Plenum Press, New York, USA, (1982).

[61] M.R. Bache, W.J. Evans, Impact of texture on mechanical properties in an advanced titanium alloy, Mater. Sci. Eng. A 319-321 (2001) 409–414.

[62] S.F. Li, B. Sun, H. Imai, K. Kondoh, Powder metallurgy Ti–TiC metal matrix composites

prepared by in situ reactive processing of Ti-VGCFs system, Carbon 61 (2013) 216–228.

[63] X.N. Mu, H.M. Zhang, H.N. Cai, Q.B. Fan, Z.H. Zhang, Y. Wu, Z.J. Fu, D.H. Yu, Microstructure evolution and superior tensile properties of low content graphene nanoplatelets reinforced pure Ti matrix composites, Mater. Sci. Eng. A 687 (2017) 164–174.

[64] J.C. Li, X.X. Zhang, L. Geng, Effect of heat treatment on interfacial bonding and strengthening efficiency of graphene in GNP/Al composites, Compos. Part A 48 (2019) 487-498.

[65] T.L. Han, J.J. Li, N.Q. Zhao, C.N. He, Microstructure and properties of copper coated graphene nanoplates reinforced Al matrix composites developed by low temperature ball milling, Carbon 159 (2020) 311-323.

[66] M.I. De Barros, D. Rats, L. Vandenbulcke, G. Farges, Influence of internal diffusion barriers on carbon diffusion in pure titanium and Ti–6Al–4V during diamond deposition, Diam. Related Mater. 8 (1999) 1022–1032.

[67] K.S. Munir, Y.F. Zheng, D.L. Zhang, J.X. Lin, Y.C. Li, C. Wen, Microstructure and mechanical properties of carbon nanotubes reinforced titanium matrix composites fabricated via spark plasma sintering, Mat. Sci. Eng. A 688 (2017) 505–523.

[68] N. Hansen, Hall-Petch relation and boundary strengthening, Scr. Mater. 51 (2004) 801-806.

[69] S.F. Li, B. Sun, H. Imai, T. Mimoto, K. Kondoh, Powder metallurgy titanium metal matrix composites reinforced with carbon nanotubes and graphite, Compos. Part A 48 (2013) 57–66.